

Phase Matching Free Sensing with Undetected Light Using a Nonlinear Metasurface

Toby Severs Millard,^{*,†,‡} Nathan Gemmell,^{*,†} Ross C. Schofield,[†] Mohsen Rahmani,[¶] Alex S. Clark,^{†,§} Chris C. Phillips,[†] and Rupert F. Oulton^{*,†}

[†]*Blackett Laboratory, Department of Physics, Imperial College London, London SW7 2AZ, UK*

[‡]*Quantum Materials Group, Quantum Technologies Department, National Physical Laboratory, Teddington TW11 0LW, UK*

[¶]*Advanced Optics & Photonics Laboratory, Department of Engineering, School of Science & Technology, Nottingham Trent University, Nottingham NG11 8NS, United Kingdom*

[§]*Quantum Engineering Technology Laboratories, University of Bristol, Bristol BS8 1QU, UK*

E-mail: t.severs-millard21@imperial.ac.uk; n.gemmell20@imperial.ac.uk; r.oulton@imperial.ac.uk

Abstract

In this letter, we report classical sensing with undetected light using octave spanning stimulated four-wave mixing from a plasmonic metasurface. The bidirectional nonlinear scattering due to inherent reflections from such thin nonlinear materials modifies their operation within a nonlinear interferometer. The theoretical model for visibility accounting for such bidirectionality as well as pulsed illumination accurately predicts visibility in the system as a function of transmission in the near-infrared seed (idler) arm. Spectrally resolving the visible signal emission evaluates the total dispersion within the interferometer, highlighting the prospect of ultrafast sensing with undetected photons.

Introduction

Nonlinear interferometry allows phase and amplitude information to be passed between light that only interacts with an object and light that is only detected.^{1–4} The interferometric technique uses correlated photon beams created in a nonlinear material, either via difference frequency generation³ or parametric fluorescence.¹ When implemented with non-degenerate beams, there are wide-reaching applications where passing information between wavelengths is desirable; for example, where the technical and fundamental limitations of mid-infrared (MIR) detectors can be circumvented with silicon-based sensors^{5–7} for label-free biological imaging,^{8,9} environmental monitoring,¹⁰ and medical imaging.^{11,12}

Recent research has predominantly focused on the quantum mechanical variant of nonlinear interferometry; where spontaneous parametric down conversion (SPDC), typically created in a bulk nonlinear crystal (NLC), interferes by induced coherence without induced emission.^{1,9,13–16} Here, indistinguishable photon pairs are generated in two paths of an interferometer such that they occupy two overlapping beam paths, labelled here as the high energy signal and the low energy idler. Induced coherence without induced emission occurs due to the lack of "which path" information; an object placed in one of the idler paths, for example, introduces path knowledge that destroys interference. What differentiates quantum nonlinear interferometry from other quantum sensing techniques, such as ghost imaging,¹⁷ is that the sensing information can be found by only detecting photons that never interacted with the object. Classical nonlinear interferometry achieves the same effect, but via stimulating the parametric fluorescence; for example, stimulating the idler while detecting the signal.^{3,4,18} The advantages of the classical variant over the quantum mechanical are improved signal-to-noise ratio and greater coherence of the bi-photon state.^{3,19}

Quantum nonlinear interferometry research has resulted in low cost and portable¹⁶ near-infrared (NIR) imaging systems at video rate^{14,20} and MIR operation.^{9,15} While the operating frequency range is set by the properties of the more common NLCs, currently achieved at up to $\sim 4\text{ }\mu\text{m}$ with 800 nm detection,¹⁵ more exotic NLCs are being explored for operation up to $10\text{ }\mu\text{m}$.^{21–23} However, crystals of order millimetres in length are required to generate sufficient levels of nonlinear

emission through phase matching techniques. Alternative media that promise range extension are nonlinear metasurfaces—subwavelength thick, nanostructured arrays that enhance nonlinear processes by supporting electromagnetic resonances with high field localisation.^{24–27} Metasurfaces can be tailor made for operation at targeted frequencies and their subwavelength thickness relaxes any phase matching and absorption constraints of the resonant nonlinearity.^{28,29} While metasurfaces outperform unpatterned films of the same thickness and material in regards to spontaneous photon pair emission rates,^{24,26} they are currently insufficient for implementing quantum nonlinear interferometry. However, by stimulating emission—and therefore operating in the classical regime—metasurfaces become suitable nonlinear sources.

Here, we demonstrate classical nonlinear interferometry to achieve phase matching free sensing with undetected photons using a resonant gold plasmonic nonlinear metasurface, where four-wave mixing (FWM) is stimulated using femtosecond pulsed pump and seed illumination. In our case, the seed beam stimulates the interferometer’s NIR idler mode to produce FWM in the visible signal mode. Amplitude and phase information of one path of the idler is observed in the visibility and phase of the signal mode interference. Operated as a folded Michelson interferometer, we study the influence of pump, seed and idler reflections combined with the bidirectional FWM emission of the metasurface. Unlike conventional nonlinear crystals, metasurface reflections cannot be eliminated due to their resonant nature. Despite these reflections and the high order nonlinearity involved, we find that the homodyne advantage leads to a signal interference visibility of over 50%. We also find signal interference independent of pump-seed delay and discuss how this can be used for ultrafast sensing with undetected light. Although experimentally implemented with a metasurface, the theoretical framework is appropriate for any thin-film nonlinear source.

Results and discussion

Nonlinear interferometry with a subwavelength source

In the Michelson-style interferometer, Fig. 1(a), FWM (signal) is generated on two pump and seed passes through the nonlinear metasurface, shown in Fig. 1(b). Pulses at 835 nm (pump, red) and

1500 nm (seed, magenta) are overlapped in transverse space at a 1 μm short-pass dichroic mirror, and in time using a piezo-controlled delay line in the seed path. Both beams are expanded to ~ 10 mm in diameter and focused using a 20 cm focal length lens to illuminate a $75 \times 75 \mu\text{m}^2$ metasurface across an areal overlap of 21 μm diameter. The metasurface is composed of gold antennas that are doubly resonant at the pump and seed wavelengths leading to enhanced electric field overlap at the incident wavelengths, generating FWM emission at 580 nm (signal, yellow) and 1500 nm (idler, magenta). Both the linear and nonlinear responses of the structures have been previously reported.^{30,31} The subwavelength thickness of the nonlinear metasurface relaxes out-of-plane phase matching, resulting in FWM (signal) in both directions on each pass, illustrated in Fig. 1(c, d). Combined with reflections of the various wavelengths from the metasurface, the nonlinear interference is distinct from conventional nonlinear interferometry.

We define the frequency domain pump and seed fields on the first pass of the metasurface as $\mathbf{E}_{p1} = E_p(\omega)\hat{x}$ and $\mathbf{E}_{s1} = E_s(\omega)\hat{y}$, respectively, where polarisation is relative to the axes marked on Fig. 1(b). FWM (signal) is generated as $\omega_f = 2\omega_p - \omega_s$. After the metasurface, the seed (idler) is separated from the pump and FWM (signal) at a 1 μm long-pass dichroic mirror, and a pair of identical curved mirrors with 20 cm radius of curvature reflect all wavelengths back along their respective paths to the metasurface. On the second pass, the returning pump field at the metasurface is $\mathbf{E}_{p2} = \sqrt{T_p}\mathbf{E}_{p1}e^{2ik_p d}$, where T_p is the metasurface pump transmission and d is the optical path length of the pump and FWM (signal) arm of the interferometer. Meanwhile the returning seed field is $\mathbf{E}_{s2} = \sqrt{T_s T}e^{i\gamma}\mathbf{E}_{s1}e^{2ik_s d'}$, where T_s is the seed transmission of the metasurface, T is the transmission coefficient and γ the phase shift of the object to be sensed, and d' is the optical path length of the interferometer's seed (idler) arm. FWM (signal) emission at each pass occurs in both $+$ and $-$ directions. The FWM field amplitude on the first pass is $\sigma_{\pm}(\omega) = \alpha_{\pm}E_p^2E_s^*$, where α_{\pm} indicates the strength of the nonlinear process, which is related to the nonlinear $\chi_{\mu\alpha\beta\gamma}^{(3)}$ tensor elements for the process. FWM (signal) on the second pass is reduced by the transmission and phase at each wavelength. We thus identify four FWM (signal) amplitudes at the metasurface per incident pump and seed pulse, illustrated and labelled in Figure 1 (c, d), and evaluate their resulting

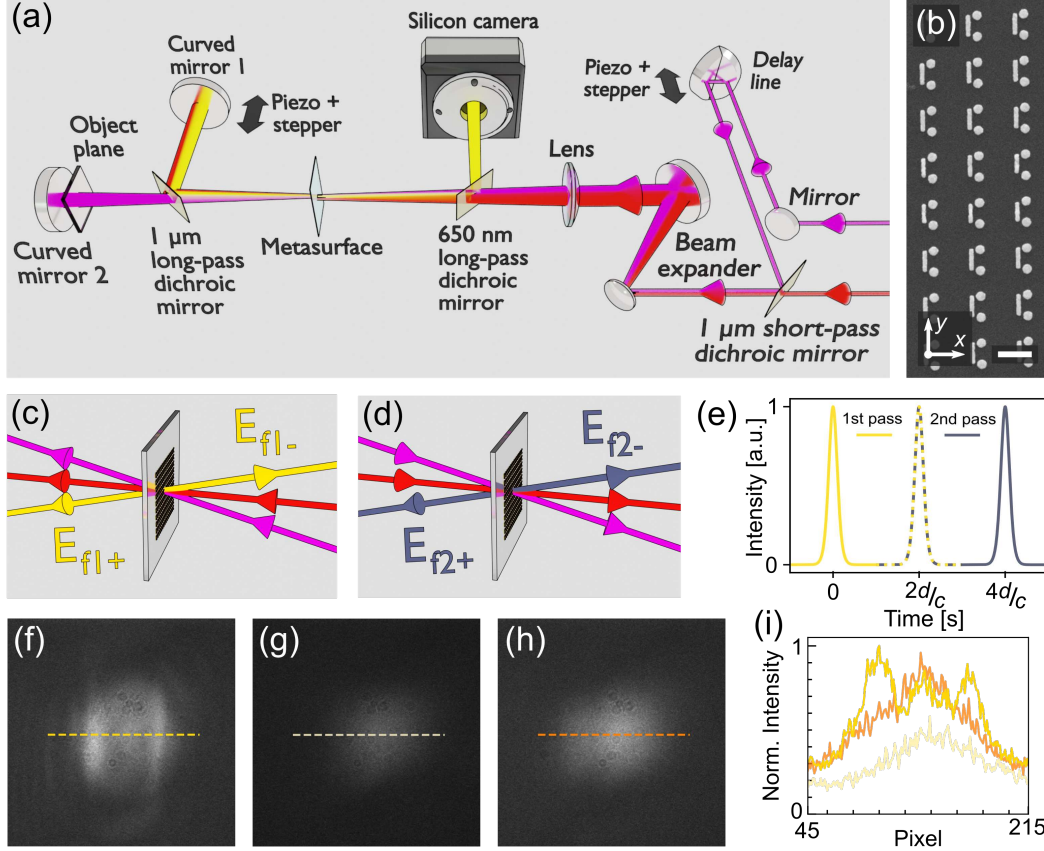


Figure 1: The interferometer system, metasurface and interference (a) The Michelson interferometer setup operating in the far field. The 835 nm pump (red) and 1500 nm seed (idler, magenta) pulsed lasers stimulate 580 nm FWM (signal, yellow). (b) SEM image the nonlinear metasurface comprised of two gold discs and a gold bar antenna per unit cell. The scale bar in 500 nm. (c, d) Graphical illustration of the bidirectional FWM (signal) emission at the first and second pass, respectively. The optical axes have been angularly displaced for clarity and do not indicate amplitude. (e) Temporal positions of FWM (signal) pulses created at each pass. The dashed lines represent E_{f1+} and E_{f2-} . Distance d is from the metasurface to curved mirror 1. (f, g, h) Intensity of FWM (signal) at the camera with no beam blocks in the interferometer arms, when beams are blocked at curved mirror 1, and when the seed (idler) is blocked at curved mirror 2, respectively. (i) Intensity at the camera along the dashed lines on (f, g, h).

amplitude and phase at the camera to be

$$E_{f1-} = \sigma_- \quad (1)$$

$$E_{f1+} = \sqrt{T_f} \sigma_+ e^{2ik_f d} \quad (2)$$

$$E_{f2-} = \sqrt{TT_p^2T_s}e^{i\gamma}\sigma_-e^{2ik_f d+i\psi} \quad (3)$$

$$E_{f2+} = \sqrt{TT_fT_p^2T_s}e^{i\gamma}\sigma_+e^{4ik_f d+i\psi} \quad (4)$$

where T_f is the metasurface FWM (signal) transmission, $2k_f(d' - d) = \psi$, is the phase difference between the interferometer's arms. The normally incident and expanded pump and seed beams ensure that the nonlinear emission is nearly in-phase across the metasurface, equivalent to matching of the in-plane momenta of the various fields, so that the longitudinal momentum is $2k_p - k_s = k_f$. The FWM (signal) is isolated from the pump and seed and directed towards a silicon camera using a 650 nm long-pass dichroic mirror. The camera thus integrates over three FWM pulses per input pump and seed pulse with relative time delays of 0, $2d/c$, $4d/c$, as illustrated in Fig. 1(e). Since the delay between distinct FWM pulses, $2d/c$, is greater than the FWM (signal) pulse duration, no interference occurs between them and the camera measures a time-averaged intensity.

$$D = |E_{f1-}|^2 + |E_{f1+} + E_{f2-}|^2 + |E_{f2+} + \sqrt{R_f}E_{f1+}e^{2ik_f d}|^2. \quad (5)$$

The third term in Eq. (5) is an interference of the forward scattered FWM (signal) from the second pass, E_{f2+} , with the forward scattered FWM (signal) from the first pass reflected by the metasurface, $\sqrt{R_f}E_{f1+}$ where R_f is the metasurface FWM reflectivity. Curved mirror 1 is connected to a second piezo-controlled stage, allowing the phase difference, ψ , to be varied. The detected signal normalised to the forward FWM emission signal, σ_+^2 , is

$$N = D/\sigma_+^2 = R_fT_f + (\eta^2 + T_f)(1 + \kappa T) + 2(\eta + \sqrt{T_fR_f})\sqrt{\kappa TT_f}\cos(\gamma + \psi), \quad (6)$$

where $\kappa = T_p^2T_s$ is the ratio of total FWM (signal) from the two passes, and $\eta = \sigma_-/\sigma_+$ is the ratio of bidirectional emission. A single frame of the FWM interference at the camera can be seen in Fig. 1(f). When a beam block is placed in front of curved mirror 1, the forward emitted first pass, E_{f1+} , is no longer detected and the pump beam does not generate FWM (signal) at the second pass, $E_{f2\pm} = 0$, so no interference is observed in Fig. 1(g), and the camera measures σ_-^2 . When the beam

block is placed in front of curved mirror 2, the seed no longer stimulates second pass emission, $E_{f2\pm} = 0$, and interference is destroyed in Fig. 1(h), so the camera records $\sigma_-^2 + (1 + R_f)T_f\sigma_+^2$. Line plots in Fig. 1(i) clarify interference and its subsequent breakdown in Fig. 1(f-h). A video of the interference fringes as ψ is varied can be found in the Supporting Information (SI). By characterising the linear transmissivity and reflectivity of each field, shown in Table I of the SI, we can evaluate the theoretical performance of the metasurface nonlinear interferometer. The expected visibility is $V = (N_{max} - N_{min}) / (N_{max} + N_{min})$ such that

$$V = \frac{2\sqrt{\kappa T T_f}(\eta + \sqrt{T_f R_f})}{R_f T_f + (\eta^2 + T_f)(1 + \kappa T)}. \quad (7)$$

At $T = 100\%$, the theoretical visibility predicts a maximum of $55.3 \pm 0.5\%$, when applying η extracted from the images in Fig. 1(g) and (h). For reference, a conventional nonlinear crystal with ideal anti-reflection coatings placed within this interferometer would only have two interfering FWM (signal) fields, $D_0 = \sigma_0^2 |E_{f1+} + E_{f2-}|^2$, which for collinear phase-matched emission, implies $\sigma_{\pm} = \sigma_0$, such that, $N_0 = 1 + T + 2\sqrt{T} \cos(\gamma + \psi)$, with a maximum visibility, $V_0 = 2\sqrt{T} / (1 + T) \mapsto 1$ in the case of no object. A more detailed derivation for the visibility can be found in Section I of the SI.

Sensing through opaque media

We compare the theoretical prediction to the experimental visibility in Fig. 2(a) with a maximum of $55.0\% \pm 11.2\%$. Here, the visibility is calculated by fitting $N = A(1 + V \cos(\phi))$ to the interference at each pixel on the camera, where ϕ is the phase and A is the DC intensity. As an interferometric technique, the corresponding phase map, Fig. 2(c), is simultaneously extracted. The saddle-like phase pattern is characteristic of interference between two fields; one diverging and the other converging. Ultimately, this condition resulting in maximised visibility is due to the same refractive lens focusing both the pump and seed to different focal points.

An advantage of non-degenerate imaging and sensing with undetected light is the ability to observe at one wavelength while exploiting the optical properties of light-matter interaction at

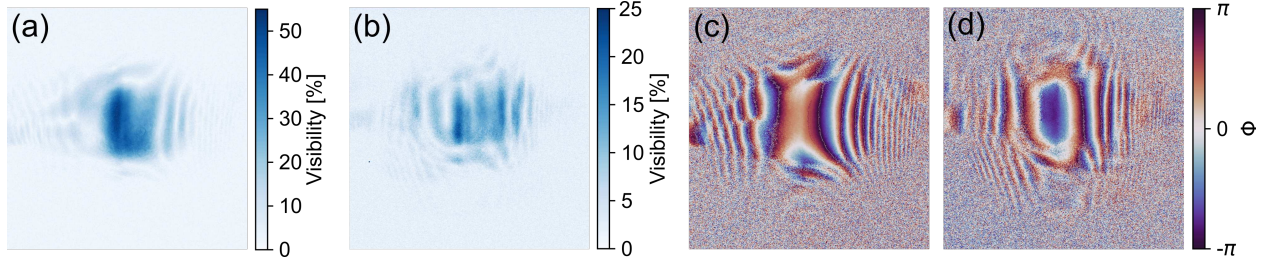


Figure 2: **Visibility and phase signal interference with and without a 240 μm Si window in the seed (idler) arm of the interferometer.** Experimental visibility at the camera with no additional material in the seed (idler) path (a) and with the silicon window (b). The corresponding phase of interference, without (c), and with (d), the silicon window in the seed (idler) arm.

another. To highlight this effect, we use the same process of extracting visibility and phase information to interference data collected through an anti-reflection coated 240 μm piece of polished Si placed at the object plane. At 580 nm, the Si window is opaque, but at 1500 nm it is measured to have a transmission of $91.2 \pm 0.9\%$, which leads to a theoretical maximum visibility of $52.3 \pm 0.5\%$ in Fig. S3(b) of the SI. In the experiment, Fig. 2(b), the visibility has dropped to a maximum of $24.4 \pm 12.2\%$. The path length introduced by the Si window is ~ 0.6 mm; greater than the coherence length of interference. Re-establishing temporal overlap is likely to have reduced nonlinear emission on the second pass, and in turn, reduced visibility. A further consequence of this realignment is that a direct measure of the phase change cannot be taken from Fig. 2(c) and (d). However, the clear pattern in (d) shows phase information is retrieved despite the reduced visibility. Additionally, the change in phase pattern suggests the focal points of the two passes have reversed from the alignment in (c).

Effect of metasurface optical properties and single-mode operation.

The derived visibility is dependent on the optical properties of the nonlinear metasurface. Visibility as a function of η , the ratio of nonlinear emission (σ_-/σ_+), shown in Fig. 3(a), peaks at $\eta = 0.67$, offset from 1 due to a trade-off between the two sets of interfering fields in Eq. (5). The first interfering term depends only on T_f while the second depends on both T_f and R_f . Therefore, maximising T_f brings the upper limit of visibility down in Fig. 3(b), while bringing the optimal

$\eta \mapsto 1$. Consequently, further optimisation could be achieved by iteratively tuning η and T_f (R_f). The ratio of total FWM (signal) emission on the second pass compared to the first is represented by the balancing term κ . As both interfering terms in Eq. (5) depend on emission from each pass, visibility is maximised at $\kappa = 1$ in Fig. 3(c). Fixing the optical parameters at the experimental and optimised values in Fig. 3(a-c) leads to the visibility curves in Fig. 3(d) as functions of the seed (idler) transmission. With this being said, an optimised metasurface may be difficult to engineer, requiring perfect transmission at the pump and seed wavelengths while balancing the bidirectionality of nonlinear emission with the reflection and transmission of FWM (signal).

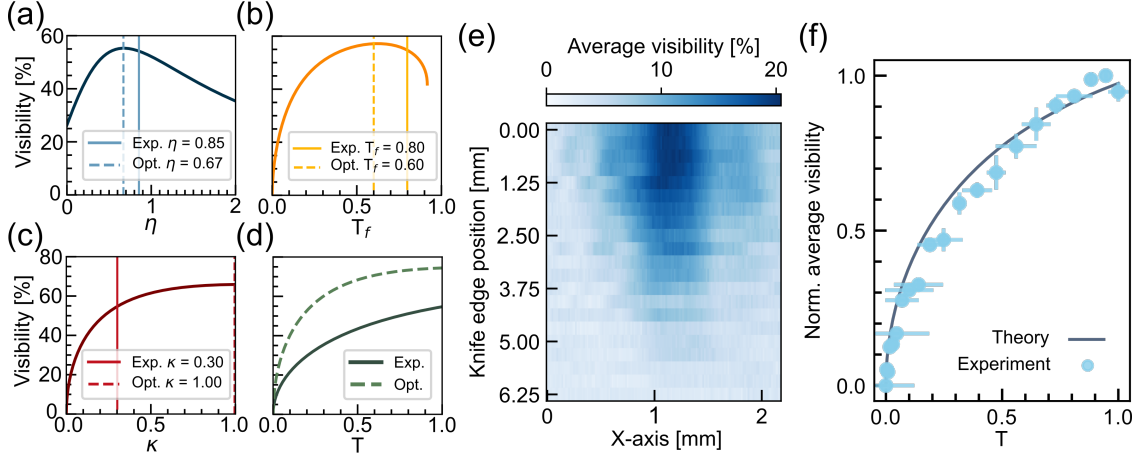


Figure 3: Visibility as functions of the average optical properties of the metasurface and transmission in the seed (idler) arm. Theoretical dependence of visibility on (a) η , (b) T_f , (c) κ and (d) seed (idler) transmission, T . The experimentally measured and optimised values are marked by the vertical lines. Constant parameters are held at the experimentally measured values in Table I of the SI. (e) Experimental average visibility across three rows of pixels, at knife edge positions that reduce seed (idler) transmission at the object plane. (f) Experimental normalised average visibility across all pixels as a function of transmission at the object plane as the knife edge is introduced. The theoretical curve uses experimentally measured optical properties as constant parameters.

In the stimulated FWM process at the metasurface the pump and seed modes generate a single idler mode. The resulting interferometer is therefore a single mode sensor and does not offer imaging capability. Any additional modes created by diffraction and/or refraction by an object do not interfere with the single mode of the first pass. By scanning a knife edge across the object plane of the interferometer we can measure a reduction of visibility, shown in Fig. 3(e). The profile

of the FWM mode remains the same shape with horizontal visibilities falling together as the seed (idler) is partially to fully obstructed. Fig. 3(f) displays the normalised visibility averaged across the entire camera sensor area, for the same experiment. The knife edge position has been converted to normalised seed (idler) transmission, T , to identify the single mode object transmission. The theoretical model predicts the visibility using the experimentally measured optical parameters of the metasurface (Table I of the SI). The visibility is normalised to account for averaging across the camera sensor.

Spectral resolution and dispersion

As the interferometer is operated with ultrafast pulses, spectral visibility and phase information are available within the FWM emission bandwidth. To access this information, the silicon camera is replaced with a spectrometer and appropriate optics. The piezo-controlled seed delay line, positioned before the 1 μm short-pass dichroic, is scanned across a 145 μm (483 fs) range with 2.5 μm (8.3 fs) steps, centred at 0 μm where the pump and seed are at their best temporal overlap that maximises the FWM (signal) emission in Fig. 4(a). The FWM (signal) spectrum blue shifts as the delay position moves from negative to positive, indicating chirp in the pump and seed pulses. The fine fringe pattern in the spectral data originates from the 175 μm thick borosilicate substrate that the metasurface sits on, which acts as a Fabry-Perot cavity. At each pump-seed delay position, the piezo-controlled curved mirror inside the interferometer is scanned across three interference fringes to extract the visibility and phase in Fig. 4(b) and (c).

Despite the clear peak in FWM (signal) emission in Fig. 4(a) the visibility in Fig. 4(b) shows a flatter profile, and a continuous phase relationship can be extracted across the entire FWM (signal) spectral range in Fig. 4(c).

The spectral shift in Fig. 4(c) shows the difference in phase between FWM (signal) generated at the first and second pass. Therefore, the phase shift comes from the combined dispersion experienced by the seed (idler), pump, and FWM (signal) after the first pass. All three pulses travel twice through the $175 \pm 13 \mu\text{m}$ borosilicate substrate of the metasurface, while the seed (idler)

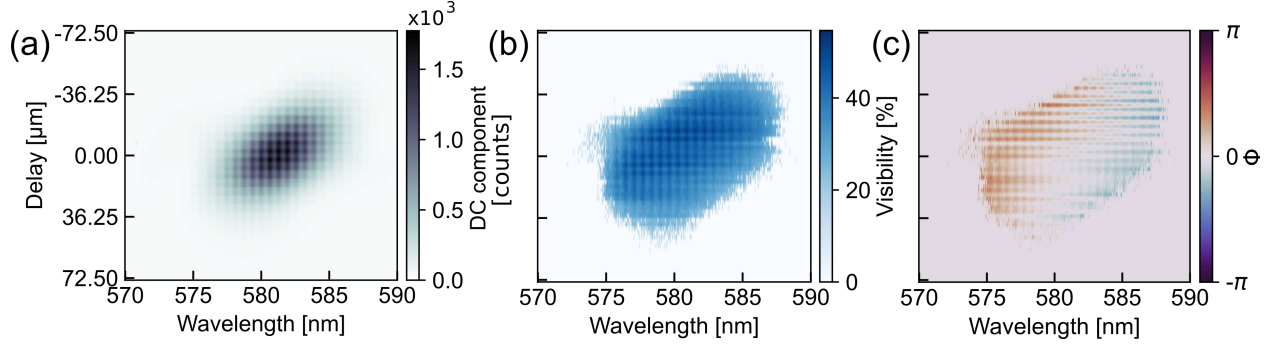


Figure 4: **2D FWM interference spectrograms for wavelength against pump-seed delay position.** (a) Intensity of the FWM (signal) DC component indicating the chirp of spectral components. (b) Spectrally resolved FWM (signal) visibility as a function of pump-seed delay, measured by scanning the interferometer idler mirror at each delay position. (c) The spectrally resolved accumulative phase from all beams as a function of pump-seed delay showing the small intrinsic dispersion of the interferometer. For (b) and (c), data extracted with a coefficient of determination, $R^2, < 0.7$ has been removed.

also travels twice through a 1 mm thick dichroic mirror nominally positioned at 45 degrees to the incoming beams. Averaging the phase shift in Figure 4 (c) across all delay positions for 575 to 585 nm gives -1.56 ± 0.29 . Importantly, the interferometer is only sensitive to variations in the object's phase, while changes in the FWM phase for different delay positions have no effect on the phase variation, as seen in Fig. 4(c). Interestingly, a Fourier transform of the interferometer visibility and phase would reveal ultrafast transients of the object transmission with a resolution less than the pulse duration.

In conclusion, we have demonstrated the operation of a nonlinear interferometer that uses a nonlinear plasmonic metasurface as a source to generate signal and idler photons through stimulated FWM to implement classical sensing with undetected light. The ability to pass amplitude and phase information from the NIR (1500 nm) to the visible (580 nm) is demonstrated by sensing through a 240 μm Si window while detecting the emission and its phase on a Si camera. Meanwhile, a knife edge was used to modulate the single-mode transmission of the interferometer. A theory of the interferometer based on any thin nonlinear source with intrinsic reflections accurately predicts the experimental visibility as a function of NIR seed (idler) transmission.

The single mode nature of interference—brought about by seeding the FWM (signal) with

single mode lasers—provides no spatial information for imaging. However, additional modes could be generated before the first pass through the metasurface. Alternatively, imaging could be achieved by adapting the interferometer to operate in real space, where the object plane is imaged onto the metasurface, which is in turn imaged onto the camera.

The spectral breadth of the signal and idler generated through pulsed illumination allows spectrally resolved visibility and phase to be measured, assessing dispersion within the interferometer. Additionally, pulsed illumination opens up avenues for ultra-fast pump-probe spectroscopy with undetected photons, such as lifetime measurements for molecular excited states and vibrations.

In combination, pulsed illumination and stimulated nonlinear emission reduce the requirement for millimetre scale exotic crystals and phase matching. The nonlinear interferometer system introduced here has the potential to reach any wavelength range where a laser and metasurface resonances are spectrally overlapped. Therefore, operation deep in the MIR ($\sim 10\ \mu\text{m}$) is conceivable, where micron scale resonators are easy to fabricate and pulsed lasers are readily available.

Methods

Sample fabrication

The metasurface was fabricated by electron beam lithography on a $175\ \mu\text{m}$ thick borosilicate glass substrate. The substrate was coated with the positive resist polymethyl methacrylate (PMMA) and baked at 180°C for at least 180 s. Nanoantenna geometries are defined by electron beam exposure at 20 keV using a $10\ \mu\text{m}$ aperture. The PMMA was developed in a 3:1 isopropyl alcohol (IPA) to methyl isobutyl ketone (MIBK) solution, and rinsed for 30 s in IPA to halt the development. A 1.5 nm adhesion layer of Cr was deposited by thermal evaporation onto the substrate, followed by 40 nm of Au (Angstrom Engineering Amod). PMMA and excess Cr/Au were removed by leaving the substrate in acetone for at least 24 hours and oxygen plasma ashing.

Optical measurements

Optical measurements were taken using a seed laser at 1500 nm (≤ 228 fs) generated by a Coherent Chameleon Compact OPO, pumped by a Coherent Chameleon Ultra II at 835 nm (≤ 146 fs). The seed was sent to a piezo-controlled delay line before being combined with the pump at a 1 μ m short-pass dichroic mirror (Thorlabs DMSP1000). Both beams were passed through a $\times 4$ reflective beam expander (Thorlabs BE04R) and focused onto the sample using a 20 cm focal length refractive lens. After the sample, the transmitted pump and forward generated FWM (signal) were separated from the seed (signal) by a 1 μ m long-pass dichroic mirror (Thorlabs DMLP1000). Identical curved mirrors, each with a 20 cm radius of curvature, reflected the respective beams back to the sample. The pump and FWM (signal) path lengths were varied by a piezo-controlled stage connected to the curved mirror in their path. A 650 nm long-pass dichroic mirror (Thorlabs DMLP650) isolated the FWM (signal) and directed it onto an EM-CCD camera (Hamamatsu C9100-23B ImagEM X2).

For spectrally resolved measurements, the camera was replaced with a 20 cm focal length lens to collimate the FWM (signal). A pinhole was used to select the centre of the interference pattern that was subsequently focused onto the entrance slit of the spectrometer (Acton SP2300) and detected on a Si-based CCD.

Data availability

Data is available upon request.

Supporting Information

Contains a detailed derivation of theory, relevant optical parameters of the metasurface, and predicted results based on these. A video of the interference pattern as the phase is shifted is also included.

Acknowledgments

T.S.M. acknowledges the support of the UK government Department for Science, Innovation and Technology through the UK National Quantum Technologies Programme and the National Physical Laboratory. This work is supported by the UK Quantum Technology Hubs in Sensing Imaging and Timing EP/Z533166/1 and Quantum Imaging EP/T00097X/1 and by the UK Engineering and Physical Sciences Research Council (EPSRC), through the Reactive Plasmonics EP/M013812/1 and Catalysis Plasmonics EP/W017075/1 Programme Grants. A.S.C acknowledges support from The Royal Society (URF/R/221019, RF/ERE/210098, RF/ERE/221060).

Author Contributions

M.R. fabricated the metasurface. T.S.M. took optical measurements. R.F.O., T.S.M. and N.G. developed the theory. T.S.M. wrote the paper with contributions from all co-authors. R.F.O., N.G., A.S.C., and C.C.P. conceived and supervised the project.

References

- (1) Lemos, G. B.; Borish, V.; Cole, G. D.; Ramelow, S.; Lapkiewicz, R.; Zeilinger, A. Quantum imaging with undetected photons. *Nature* **2014**, *512*, 409–412.
- (2) Lahiri, M.; Lapkiewicz, R.; Lemos, G. B.; Zeilinger, A. Theory of quantum imaging with undetected photons. *Phys. Rev. A* **2015**, *92*, 013832.
- (3) Cardoso, A. C.; Berruezo, L. P.; Ávila, D. F.; Lemos, G. B.; Pimenta, W. M.; Monken, C. H.; Saldanha, P. L.; Pádua, S. Classical imaging with undetected light. *Phys. Rev. A* **2018**, *97*, 033827.
- (4) Shapiro, J. H.; Venkatraman, D.; Wong, F. N. C. Classical Imaging with Undetected Photons. *Scientific Reports* **2015**, *5*, 10329.

- (5) Rogalski, A.; Martyniuk, P.; Kopytko, M. Challenges of small-pixel infrared detectors: a review. *Reports on Progress in Physics* **2016**, 79, 046501.
- (6) Lindner, C.; Wolf, S.; Kiessling, J.; Kühnemann, F. Fourier transform infrared spectroscopy with visible light. *Opt. Express* **2020**, 28, 4426–4432.
- (7) Lindner, C.; Kunz, J.; Herr, S. J.; Kießling, J.; Wolf, S.; Kühnemann, F. High-sensitivity quantum sensing with pump-enhanced spontaneous parametric down-conversion. *APL Photonics* **2023**, 8, 051301.
- (8) Greaves, G. E.; Kiryushko, D.; Auner, H. W.; Porter, A. E.; Phillips, C. C. Label-free nanoscale mapping of intracellular organelle chemistry. *Communications Biology* **2023**, 6, 583.
- (9) Kviatkovsky, I.; Chrzanowski, H. M.; Avery, E. G.; Bartolomaeus, H.; Ramelow, S. Microscopy with undetected photons in the mid-infrared. *Science Advances* **2020**, 6, eabd0264.
- (10) Pejčic, B.; Myers, M.; Ross, A. Mid-Infrared Sensing of Organic Pollutants in Aqueous Environments. *Sensors* **2009**, 9, 6232–6253.
- (11) Amrania, H.; Woodley-Barker, L.; Goddard, K.; Rosales, B.; Shousha, S.; Thomas, G.; McFarlane, T.; Sroya, M.; Wilhelm-Benartzi, C.; Cocks, K.; Coombes, R. C.; Phillips, C. C. Mid-infrared imaging in breast cancer tissue: an objective measure of grading breast cancer biopsies. *Convergent Science Physical Oncology* **2018**, 4, 025001.
- (12) Contreras-Rozo, J. A.; Mata-Miranda, M. M.; Vazquez-Zapien, G. J.; Delgado-Macuil, R. J. Infrared spectroscopy technique: An alternative technology for diabetes diagnosis. *Biomedical Signal Processing and Control* **2023**, 86, 105246.
- (13) Wang, L. J.; Zou, X. Y.; Mandel, L. Induced coherence without induced emission. *Phys. Rev. A* **1991**, 44, 4614–4622.

- (14) Gilaberte Basset, M.; Hochrainer, A.; Töpfer, S.; Riexinger, F.; Bickert, P.; León-Torres, J. R.; Steinlechner, F.; Gräfe, M. Video-Rate Imaging with Undetected Photons. *Laser & Photonics Reviews* **2021**, *15*, 2000327.
- (15) Kviatkovsky, I.; Chrzanowski, H. M.; Ramelow, S. Mid-infrared microscopy via position correlations of undetected photons. *Opt. Express* **2022**, *30*, 5916–5925.
- (16) Pearce, E.; Gemmell, N. R.; Flórez, J.; Ding, J.; Oulton, R. F.; Clark, A. S.; Phillips, C. C. Practical quantum imaging with undetected photons. *Opt. Continuum* **2023**, *2*, 2386–2397.
- (17) Erkmen, B. I.; Shapiro, J. H. Ghost imaging: from quantum to classical to computational. *Adv. Opt. Photon.* **2010**, *2*, 405–450.
- (18) Huang, M.; Wu, D.; Ren, H.; Shen, L.; Hawkins, T. W.; Ballato, J.; Gibson, U. J.; Beresna, M.; Slavík, R.; Sipe, J. E.; Liscidini, M.; Peacock, A. C. Classical imaging with undetected photons using four-wave mixing in silicon core fibers. *Photon. Res.* **2023**, *11*, 137–142.
- (19) Kolobov, M. I.; Giese, E.; Lemieux, S.; Fickler, R.; Boyd, R. W. Controlling induced coherence for quantum imaging. *Journal of Optics* **2017**, *19*, 054003.
- (20) Pearce, E.; Wolley, O.; Mekhail, S. P.; Gregory, T.; Gemmell, N. R.; Oulton, R. F.; Clark, A. S.; Phillips, C. C.; Padgett, M. J. Single-frame transmission and phase imaging using off-axis holography with undetected photons. *Scientific Reports* **2024**, *14*, 16008.
- (21) Kumar, M.; Kumar, P.; Vega, A.; Weissflog, M. A.; Pertsch, T.; Setzpfandt, F. Mid-infrared photon pair generation in AgGaS₂. *Applied Physics Letters* **2021**, *119*, 244001.
- (22) Paterova, A. V.; Toa, Z. S. D.; Yang, H.; Krivitsky, L. A. Broadband Quantum Spectroscopy at the Fingerprint Mid-Infrared Region. *ACS Photonics* **2022**, *9*, 2151–2159.
- (23) Mukai, Y.; Okamoto, R.; Takeuchi, S. Quantum Fourier-transform infrared spectroscopy in the fingerprint region. *Opt. Express* **2022**, *30*, 22624–22636.

- (24) Santiago-Cruz, T.; Fedotova, A.; Sultanov, V.; Weissflog, M. A.; Arslan, D.; Younesi, M.; Pertsch, T.; Staude, I.; Setzpfandt, F.; Chekhova, M. Photon Pairs from Resonant Metasurfaces. *Nano Letters* **2021**, *21*, 4423–4429, PMID: 33971095.
- (25) Santiago-Cruz, T.; Gennaro, S. D.; Mitrofanov, O.; Addamane, S.; Reno, J.; Brener, I.; Chekhova, M. V. Resonant metasurfaces for generating complex quantum states. *Science* **2022**, *377*, 991–995.
- (26) Son, C.; Sultanov, V.; Santiago-Cruz, T.; Anthur, A. P.; Zhang, H.; Paniagua-Dominguez, R.; Krivitsky, L.; Kuznetsov, A. I.; Chekhova, M. V. Photon pairs bi-directionally emitted from a resonant metasurface. *Nanoscale* **2023**, *15*, 2567–2572.
- (27) Zhang, J.; Ma, J.; Li, N.; Lung, S.; Sukhorukov, A. A. Single-shot characterization of photon indistinguishability with dielectric metasurfaces. *Optica* **2024**, *11*, 753–758.
- (28) Schulz, S. A. et al. Roadmap on photonic metasurfaces. *Applied Physics Letters* **2024**, *124*, 260701.
- (29) Oulton, R. F.; Flórez, J.; Clark, A. S. Ferroelectric nanosheets boost nonlinearity. *Nature Photonics* **2022**, *16*, 611–612.
- (30) Gennaro, S. D.; Rahmani, M.; Giannini, V.; Aouani, H.; Sidiropoulos, T. P. H.; Navarro-Cía, M.; Maier, S. A.; Oulton, R. F. The Interplay of Symmetry and Scattering Phase in Second Harmonic Generation from Gold Nanoantennas. *Nano Letters* **2016**, *16*, 5278–5285, PMID: 27433989.
- (31) Gennaro, S. D.; Li, Y.; Maier, S. A.; Oulton, R. F. Double Blind Ultrafast Pulse Characterization by Mixed Frequency Generation in a Gold Antenna. *ACS Photonics* **2018**, *5*, 3166–3171.

Phase Matching Free Sensing with Undetected Light Using a Nonlinear Metasurface: Supporting Information

SI. ANALYTICAL VISIBILITY DERIVATION

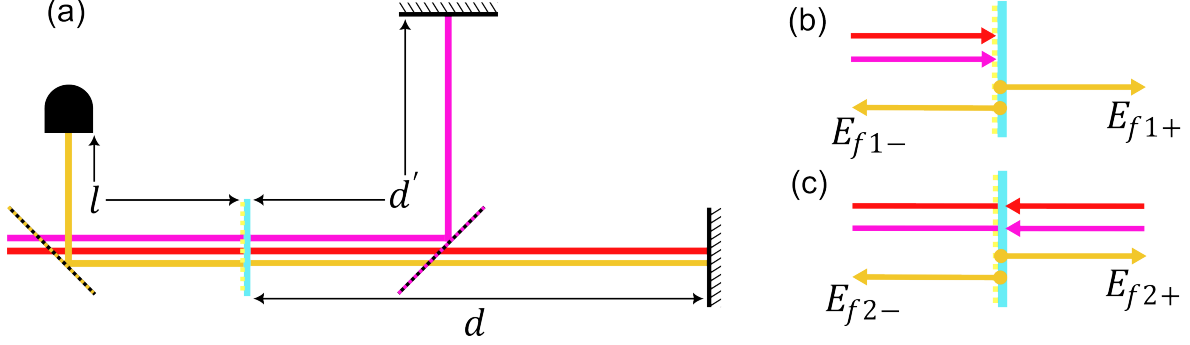


Figure S1: **A simplified schematic of the interferometer system shown in Fig. 1(a) of the main text, to support the derivation below.** (a) Beam paths of the pump (red), seed (idler, magenta) and FWM (signal, yellow) with the path lengths labelled. Due to the relaxation of out-of-plane phase matching requirements, FWM signal is emitted in both the + and - directions at the (b) first and (c) second pass. This, combined with pulsed illumination, creates temporal windows where interference can occur.

At the first pass through the metasurface the amplitude and phase of the pump and seed fields are described, respectively, by

$$E_{p1} = E_p(\omega)e^{i\phi_p(\omega)} \text{ and} \quad (1)$$

$$E_{s1} = E_s(\omega)e^{i\phi_s(\omega)}. \quad (2)$$

Here, $E_{p,s}(\omega)$ and $\phi_{p,s}(\omega)$ are the frequency dependent amplitude and phase of the pump and seed. After travelling the paths shown in Fig. S1, the fields at the second pass become

$$E_{p2} = t_p E_{p1} e^{2ik_p d} \text{ and} \quad (3)$$

$$E_{s2} = t_s t e^{i\gamma} E_{s1} e^{2ik_s d'}. \quad (4)$$

Where $t_{p,s}$ are the pump and seed transmission amplitudes through the metasurface and it is assumed the dichroic mirror is perfectly reflective for the pump and FWM, and is perfectly transmissive for the seed (idler). The seed (idler) beam passes through an object or material with transmission t , inducing a phase shift of γ .

Due to the subwavelength thickness, the phase matching requirements are relaxed and FWM (signal) is emitted out of the metasurface plane in both directions. However, due to the different refractive indices of the sub- and superstrate, the strength of emission is not equal in each direction relative to the metasurface (+ and -). We define FWM (signal) by the input beams,

$$E_{f1\pm, f2\pm} = \alpha_{\pm} E_{p1, p2}^2 E_{s1, p2}^*, \quad (5)$$

where α_{\pm} indicates the strength of the nonlinear process, which is related to the nonlinear $\chi_{\mu, xy}^{(3)}$ tensor elements for the process. We are working under the assumption of undepleted beams, such that after FWM generation the pump and seed amplitudes are unchanged.

FWM fields generated at each pass and each direction are then evaluated at the detector using Eqs. (3-5) and path distances within the interferometer outlined in Fig. S1,

$$E_{f1+} = t_f \alpha_+ E_{p1}^2 E_{s1}^* e^{ik_f(2d+l)} \quad (6)$$

$$E_{f1-} = \alpha_- E_{p1}^2 E_{s1}^* e^{ik_f l} \quad (7)$$

$$E_{f2+} = \alpha_+ E_{p2}^2 E_{s2}^* e^{ik_f(d+l)} = t_f t e^{i\gamma} \alpha_+ t_p^2 t_s E_{p1}^2 E_{s1}^* e^{ik_f(d+l)-2ik_s d' + 4ik_p d} \quad (8)$$

$$E_{f2-} = \alpha_- E_{p2}^2 E_{s2}^* e^{ik_f l} = t e^{i\gamma} \alpha_- t_p^2 t_s E_{p1}^2 E_{s1}^* e^{ik_f l - 2ik_s d' + 4ik_p d}. \quad (9)$$

Here, t_f is the transmission amplitude of the metasurface at the FWM wavelength. To simplify the above equations we introduce the average nonlinear amplitude in each direction at either pass, σ_{\pm} ,

$$\alpha_{\pm} E_p^2 E_s^* e^{ik_f l} e^{i(2\phi_p(\omega) - \phi_s(\omega))} = \Sigma_{\pm}(\omega) e^{i\phi_f(\omega)} = \sigma_{\pm}, \quad (10)$$

where $\Sigma_{\pm}(\omega)$ represents the frequency dependent nonlinear amplitude. We then consider conservation of energy and momentum

$$2\omega_p - \omega_s = \omega_f \Rightarrow 2k_p - k_s = k_f, \quad (11)$$

and relate the path lengths of the interferometer's arms

$$d' = d + \delta \quad (12)$$

$$2k_s \delta = \psi. \quad (13)$$

δ is the path difference between the interferometer arms that leads to a phase difference of ψ on the seed (idler). Substituting Eqs. (10-13) into Eqs. (7-8) leads to

$$E_{f1+} = t_f \sigma_+ e^{2ik_f d} \quad (14)$$

$$E_{f1-} = \sigma_- \quad (15)$$

$$E_{f2+} = tt_ft_s t_p^2 \sigma_+ e^{i\gamma} e^{4ik_f d + i\psi} \quad (16)$$

$$E_{f2-} = tt_s t_p^2 \sigma_- e^{i\gamma} e^{2ik_f d + i\psi}. \quad (17)$$

Across Eqs. (14-17) there are three windows in time at which FWM (signal) reaches the detector, separated by the time taken for light to traverse the interferometer 0, $2k_f d$ and $4k_f d$. The coherence time of these temporal windows are limited by the shortest pulse duration in our system ($\tau_p \approx 150$ fs[1]). As $2k_f d \gg c\tau_p$ and the repetition rate of the laser, 80 MHz, is mismatched with the interferometer arm lengths, ~ 20 cm, only light arriving within the same temporal window will interfere. Therefore, when calculating the intensity at the detector, D , light arriving within the same temporal window are grouped together

$$D = |E_{f1-}|^2 + |E_{f1+} + E_{f2-}|^2 + |E_{f2+} + E_{f1+} r_f e^{2ik_f d}|^2. \quad (18)$$

An additional term has been included due to the back reflection of E_{f1+} off the metasurface leading to a temporal overlap with E_{f2+} at $4k_f d$. Substituting in the amplitudes in Eqs. (14-17) and normalising the detected signal, $N = D/\sigma_+^2$, relative to the forward FWM emission signal, σ_+^2 gives us

$$N = R_f T_f + (\eta^2 + T_f)(1 + \kappa T) + 2(\eta + \sqrt{T_f R_f})\sqrt{\kappa T T_f} \cos(\gamma + \psi), \quad (19)$$

Where $T = t^2$, $\kappa = T_p^2 T_s$ is ratio of total FWM (signal) from the two passes, and $\eta = \sigma_-/\sigma_+$ is the ratio of emission in the backwards and forwards directions. Calculating visibility as $V = \frac{N_{max} - N_{min}}{N_{max} + N_{min}}$ gives

$$V = \frac{2\sqrt{\kappa T T_f}(\eta + \sqrt{T_f R_f})}{R_f T_f + (\eta^2 + T_f)(1 + \kappa T)}. \quad (20)$$

SII. EXPERIMENTAL OPTICAL PARAMETERS

Transmission and reflection measurements were taken with the same tuneable pulsed laser as used for the main experiment at 835, 1500 for the pump and seed (idler), respectively. For measurements at 580 nm, the seed was tuned to 1160 nm and passed through a frequency doubler. The FWM (signal) emission in each direction, σ_{\pm} , was extracted from the intensities at the camera seen in Fig. S2(a) and (b) (Fig. 1(g) and (h) of the main text), using constants from Table I. The visibility in Table I was calculated from all extracted parameters using Eq. (20) and represents an average across the detector.

Parameter	Label	Value	Uncertainty (\pm)
Metasurface pump transmission	T_p	0.784	0.002
Metasurface seed transmission	T_s	0.47	0.01
Metasurface FWM transmission	T_f	0.80	0.03
Metasurface FWM reflection	R_f	0.118	0.002
Normalised FWM emission in + direction	σ_+	0.546	0.001
Normalised FWM emission in - direction	σ_-	0.454	0.001
FWM emission ratio (σ_-/σ_+)	η	0.854	0.002
Average visibility	V	0.54	0.01

TABLE I: **Experimentally measured optical parameters for calculating visibility.**

SIII. PREDICTED VISIBILITY

As mentioned above, the predicted visibility is calculated from images of the non-interfering fields at the camera, when a beam block is placed in respective arms of the interferometer. Fig. S2(a) and (b) shows these images labelled with the combination of FWM fields and linear optical properties of the metasurface that define them. Far-field images of σ_{\pm} and η calculated from Fig. S2(a) and (b) are seen in (c-e). The far-field measurement of η is then used to predict the visibility across the camera using the parameters of the characterised metasurface to give Fig. S3 (a). The transmission of one pass through the Si window was measured directly to be $91.3 \pm 0.9\%$ at 1500 nm, and was subsequently used to calculate Fig. S3 (b). Here, the increase in optical path length due to the Si window—in turn reducing visibility—has not been considered.

-
- [1] S. D. Gennaro, Y. Li, S. A. Maier, and R. F. Oulton, Double blind ultrafast pulse characterization by mixed frequency generation in a gold antenna, ACS Photonics **5**, 3166 (2018), <https://doi.org/10.1021/acsphotonics.8b00387>.

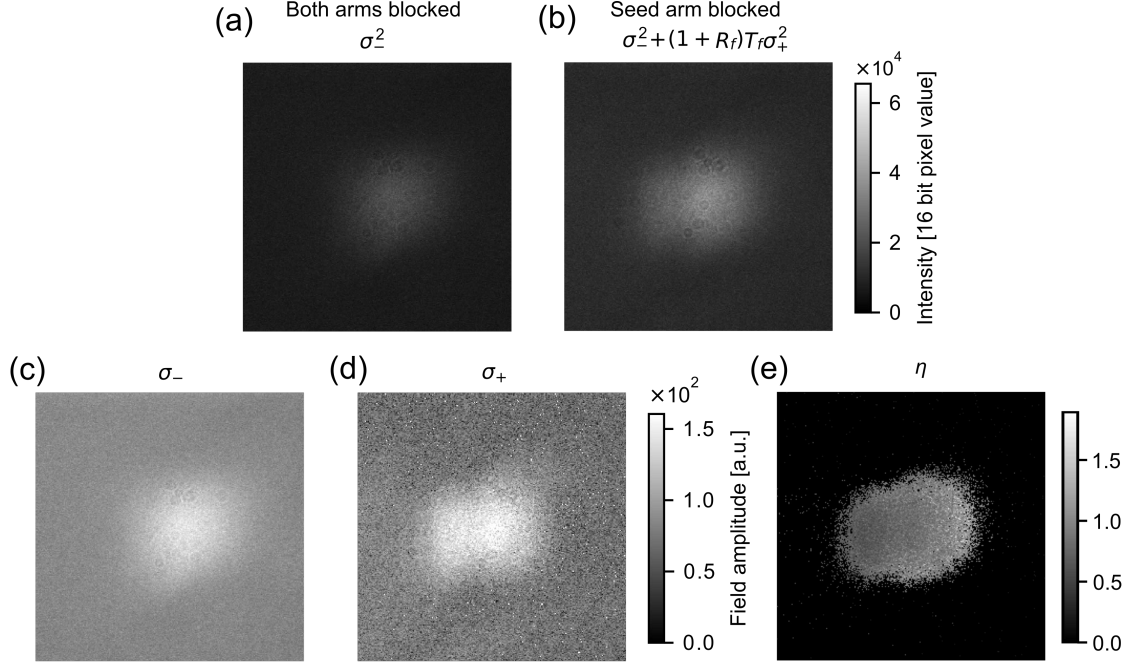


Figure S2: **Extracted amplitudes of bidirectional FWM emission and η .** (a) Camera response to only first pass reflected emission, E_{f1-} . (b) Camera response to the reflected, E_{f1-} , and transmitted, E_{f1+} , first pass emission. Amplitude of FWM emission at the metasurface in the (c) $-$ and (d) $+$ direction. (e) η calculated from (c) and (d). A threshold has been applied to improve clarity.

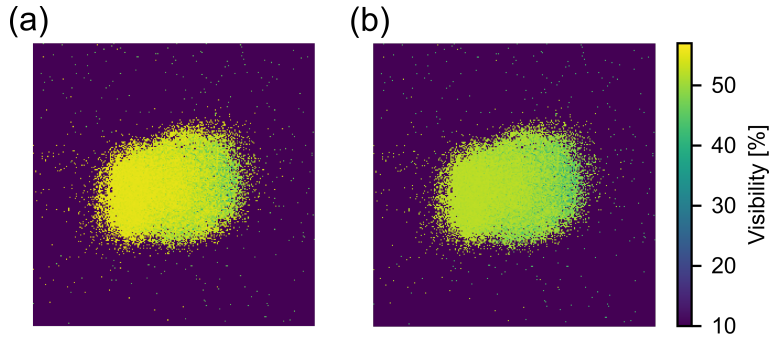


Figure S3: **Expected visibility from extracted η and linear optical properties of the metasurface in Table I.** (a) Calculated visibility when $T=100\%$. (b) Calculated visibility when $T=83\pm 3\%$; the measured transmission of two passes through the $240\ \mu\text{m}$ thick Si window at $1500\ \text{nm}$.